JOURNAL OF GEOPHYSICAL RESEARCH, VOL. 115, B02201, doi:10.1029/2009JB006329, 2010

First principles study of thermodynamics and phase transition in low-pressure ($P2_1/c$) and high-pressure ($C2/c$) clinoenstatite $MgSiO_3$

Yonggang G. Yu,[1,2] Renata M. Wentzcovitch,[3] and Ross J. Angel[4]

Received 25 January 2009; revised 27 April 2009; accepted 14 September 2009; published 4 February 2010.

[1] Using first principles quasi-harmonic theory, we have investigated the vibrational and thermodynamic properties of $P2_1/c$ and $C2/c$ $MgSiO_3$ clinoenstatites. Very good agreement between experimentally measured thermodynamic properties, such as equation of state, and those predicted by the local density approximation (LDA) functional has been found. The level of agreement found in these chain silicates is comparable to that found in framework silicates such as $MgSiO_3$ perovskite. The phase boundaries calculated by the LDA and the generalized gradient approximation (GGA) bracket the experimentally measured ones following the established trend that the GGA functional overestimates the transition pressure while the LDA functional underestimates it. The calculated Clapeyron slope is 2.9 MPa K^{-1} and is used to constrain the position of the 3-pyroxene ($P2_1/c$, $C2/c$, and Pbca) triple point in $MgSiO_3$, with the aid of room temperature experimental hysteresis in the $P2_1/c$ to $C2/c$ transition.

Citation: Yu, Y. G., R. M. Wentzcovitch, and R. J. Angel (2010), First principles study of thermodynamics and phase transition in low-pressure ($P2_1/c$) and high-pressure ($C2/c$) clinoenstatite $MgSiO_3$, *J. Geophys. Res.*, *115*, B02201, doi:10.1029/2009JB006329.

1. Introduction

[2] Pyroxenes, including clinopyroxenes with $P2_1/c$ and $C2/c$ symmetries and orthopyroxene with Pbca symmetry, are important constituents of the Earth's upper mantle [*Ringwood*, 1975]. Unlike the olivine group minerals (olivine, wadsleyite, and ringwoodite) in which the dominant cations are Mg and Fe, pyroxenes host a variety of elements, such as Mg, Ca, Al, Fe, Mn, Na, and K, forming extensive solid solutions. Among these are some end-members such as $Mg_2Si_2O_6$ enstatite, $Fe_2Si_2O_6$ ferrosilite, $MgCaSi_2O_6$ diopside, and $NaAlSi_2O_6$ jadeite, to name a few. Thermodynamic properties of these minerals should influence upper mantle convection, while phase transitions in pyroxenes may be related to seismic discontinuities in the upper mantle. For example, *Woodland and Angel* [1997]; *Woodland* [1998] suggested that the orthopyroxene to high-pressure clinopyroxene transition could account for the X discontinuity at 312 ± 21 km depth reported by *Revenaugh and Jordan* [1991]. The extensive dissolution of pyroxene into garnet can enhance the positive velocity gradient at depths of 300–460 km in the Earth [*Ringwood*, 1967]. Therefore, it is of fundamental importance to understand thermodynamic properties of pyroxenes at upper mantle conditions.

[3] At low pressures $MgSiO_3$ enstatite exists mainly in two polymorphs, Pbca orthoenstatite stable at higher temperatures and low-pressure clinoenstatite with $P2_1/c$ symmetry (hereafter LP-En) at lower temperatures. Indirect experimental evidence of the existence of a high-pressure $C2/c$ $MgSiO_3$ enstatite (hereafter HP-En) had appeared in the literature since 1970s as the result of studies of the inversion of orthoenstatite to a higher-pressure phase [*Akaogi and Akimoto*, 1977; *Pacalo and Gasparik*, 1990; *Kanzaki*, 1991] which was recovered from quenched samples as LP-En. An in situ high-pressure single-crystal X-ray study by *Angel et al.* [1992] revealed a nonquenchable pressure-induced phase transition between LP-En and HP-En and determined the crystal structure of HP-En. Confirmation of the phase transition was also provided from a Raman spectroscopy study by *Chopelas and Boehler* [1992].

[4] Volume versus pressure equations of state for LP-En and HP-En at room temperature [*Angel and Hugh-Jones*, 1994; *Kung et al.*, 2004] and at elevated temperatures [*Shinmei et al.*, 1999] have been reported. Only limited Raman and IR spectroscopy of LP-En and HP-En are available [*Chopelas and Boehler*, 1992; *Chopelas*, 1999; *Lin*, 2004], and there is little data on the thermodynamic properties such as the pressure-temperature dependence of thermal expansion coefficients and heat capacity [*Krupka et al.*, 1985]. In the past two decades a few theoretical studies have been reported in the literature, including density functional theory (DFT) studies of the static equation of state of HP-En and LP-En [*Wentzcovitch et al.*, 1995; *Duan et al.*, 2001]; empirical potential based molecular dynamics (MD) study [*Matsui and Price*, 1992; *Shimobayashi et al.*, 2001],

[1]Department of Chemistry, Minnesota Supercomputing Institute, University of Minnesota, Minneapolis, Minnesota, USA.
[2]Now at Department of Geosciences, Virginia Polytechnic Institute and State University, Blacksburg, Virginia, USA.
[3]Department of Chemical Engineering and Materials Science, Minnesota Supercomputing Institute, University of Minnesota, Minneapolis, Minnesota, USA.
[4]Department of Geosciences, Virginia Polytechnic Institute and State University, Blacksburg, Virginia, USA.

0148-0227/10/2009JB006329$09.00

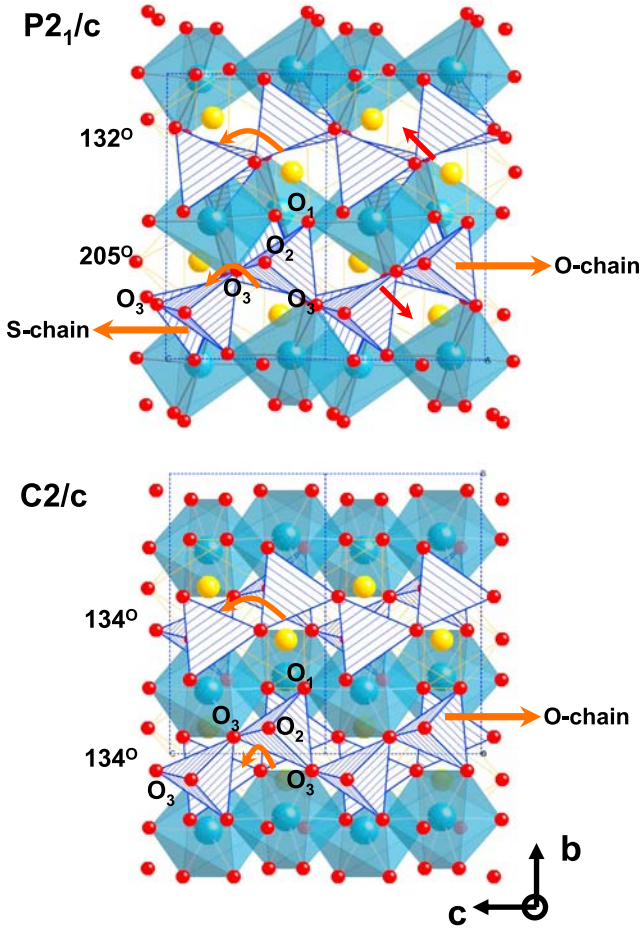

Figure 1. Crystal structures of (top) $MgSiO_3$ LP-En ($P2_1/c$) and (bottom) HP-En (C2/c) at 0 GPa (static LDA results). One viable transition path is shown by red arrows in Figure 1 (top), which draws the S chain away from the O chain parallel to *bc* plane. The magnesium M1 sites are represented by octahedra and M2 by solid yellow circles. (Atom coordinates in Table 2.)

lattice dynamics study [*Mendelssohn and Price*, 1997; *Choudhury et al.*, 1998], topology analysis of pyroxene crystal structures from procrystal electron density [*Downs*, 2003], and simulation of the structural variation of orthoenstatite at high pressures [*Jahn*, 2008; *Jahn and Martoňák*, 2008] by metadynamics [e.g., *Martoňák et al.*, 2006]. However, previous DFT studies contain only the 0 K static results. While previous MD simulations and lattice dynamics calculations can produce qualitatively good agreement with experimentally measured thermodynamic properties, the accuracy is insufficient to determine phase boundaries. Pseudopotential-based DFT calculation in conjunction with the quasi-harmonic approximation (QHA), as described by *Karki et al.* [2000], has previously been applied to the Mg_2SiO_4 system at upper mantle and transition zone conditions. Those calculations reproduced successfully both experimentally measured thermodynamic properties [*Yu and Wentzcovitch*, 2006; *Li et al.*, 2007; *Wu and Wentzcovitch*, 2007] and phase stability fields including Clapeyron slopes [*Yu et al.*, 2007, 2008] in Mg_2SiO_4. Here we report a thorough first principles study of the lattice dynamic properties of LP-En and HP-En. From the predicted vibrational density of states of both phases at various pressures we derive their thermodynamic properties within the QHA, and determine the slope of the phase boundary between them.

2. Computational Method

[5] Computations were performed in primitive cells with 40 and 20 atoms for LP-En and HP-En, respectively. Our density functional calculations use the Perdew-Burke-Ernzerhof (PBE) generalized gradient approximation (GGA) [*Perdew et al.*, 1996] and Ceperley-Alder local density approximation (LDA) [*Ceperley and Alder*, 1980] as parameterized by *Perdew and Zunger* [1981] for exchange correlation functionals in combination with the plane wave pseudopotential method as implemented in the Quantum ESPRESSO package [*Giannozzi et al.*, 2009]. The LDA in conjunction with the QHA predicts high-temperature structural properties that are in better agreement with experimental measurements than the GGA. The pseudopotentials used here have been used in previous studies of magnesium silicates [*Tsuchiya et al.*, 2004]. The *Troullier and Martins* [1991] magnesium pseudopotential used in previous studies [*Wentzcovitch et al.*, 1995; *Duan et al.*, 2001] was replaced by a more transferable one generated by the method of U. von Barth and R. Car (unpublished data, briefly described by *Dal Corso et al.* [1993]). Those for oxygen and silicon were generated by the method of *Troullier and Martins* [1991]. The plane wave kinetic energy cutoff (E_{cut}) was chosen to be 80 Ry, and a $4 \times 4 \times 4$ (with $(\frac{1}{2}\frac{1}{2}\frac{1}{2})$ shift from origin) Monkhorst-Pack k point mesh [*Monkhorst and Pack*, 1976] was used for Brillouin zone (BZ) samplings of electronic states for both phases. The resulting energy convergence with respect to E_{cut} and k mesh is within 1.5×10^{-4} Ry atom^{-1}. Structural relaxations at constant pressure were performed using variable-cell shape molecular dynamics [*Wentzcovitch*, 1991; *Parrinello and Rahman*, 1980], as in previous studies [*Wentzcovitch et al.*, 1995; *Duan et al.*, 2001]. The dynamical matrix was computed on a $2 \times 2 \times 2$ q point grid at all volumes using density functional perturbation theory [*Baroni et al.*, 2001]. It was then interpolated to a denser $8 \times 8 \times 8$ q point mesh for both LP-En and HP-En. This corresponds to molecular dynamics simulations using 20,480 (10,240) atoms for LP-En (HP-En) phase. The eigenvalues of the dynamical matrix, i.e., square of phonon frequencies, in the denser q mesh then produced phonon dispersions and vibrational density of states for computations of thermodynamic properties.

3. Crystal Structure and Lattice Vibrations

[6] Both LP-En ($P2_1/c$) and HP-En (C2/c) exist in monoclinic structures with the unique axis *b* perpendicular to the other two axes, *a* and *c* (Figure 1). The obtuse monoclinic angle, β, between *a* and *c*, is about 108° for LP-En (ambient conditions) and 101° for HP-En (7.9 GPa). What makes pyroxene of special interest are the corner sharing silicate tetrahedral chains running through the crystal along the $\hat{c}$ axis, forming silicate layers parallel to the *b*-*c* plane. There are two symmetrically distinct tetrahedral chains in LP-En. By convention these are labeled "O-rotated" chain (O chain) and "S-rotated" chain (S chain) based on the O_3-O_3-O_3 chain

Table 1. Calculated Unit Cell Parameters (Static LDA) Compared With Experiments for LP-En (Ambient Condition) and HP-En (7.9 GPa) in $MgSiO_3$

	a (Å)	b (Å)	c (Å)	β (deg)	V(Å^3)
		LP-En			
This work	9.544	8.755	5.140	107.78	409.0
Ohashi [1984]	9.606	8.8131	5.170	108.35	415.5
Matsui and Price [1992]	9.600	8.672	5.244	108.60	413.8
Duan et al. [2001]	9.487	8.668	5.105	107.90	399.5
Jahn [2008]	9.45	8.68	5.09	108.0	397.1
		HP-En			
This work	9.167	8.60	4.90	101.0	379.1
Wentzcovitch et al. [1995]	9.12	8.19	4.904	101.3	359.2
Angel et al. [1992]	9.201	8.621	4.908	101.50	381.5

extension angle (Figure 1). The S chain in LP-En has an O_3-O_3-O_3 angle of ~205°, and the O chain has an angle of ~132° at ambient pressure. There is only one symmetrically distinct chain in HP-En, with an "O"-type rotation and an angle ~134° (0 GPa calculation).

[7] The calculated static crystal cell parameters and internal Wyckoff positions are compared with those from previous calculations and experiments in Tables 1 and 2. These cell parameters and unit cell volumes agree better with experiments [*Ohashi*, 1984; *Angel et al.*, 1992] than previous results by *Duan et al.* [2001]; *Jahn* [2008] and *Wentzcovitch et al.* [1995]. The previous molecular dynamics study of LP-En by *Matsui and Price* [1992] that employed empirical potentials had produced unit cell volumes and β angle in very good agreement with experiments, but complete thermodynamic properties were not obtained. Here we calculate phonon dispersions and vibrational density of states for LP-En and HP-En and visualize [*Kokalj*, 2003] some low-frequency vibrational modes.

[8] The unit cell of LP-En contains 8 formula units (40 atoms), so there are 120 normal modes for each point in the Brillouin zone, among which 3 are acoustic (1 longitudinal (LA) and 2 transverse (TA)) and 117 are optical (39 longitudinal (LO) and 78 transverse (TO)). The optical modes at the BZ center may be divided by symmetry [*Capillas et al.*, 2003] as

$$\Gamma^{\text{disp}} = 30\text{A}_\text{g}(\text{R}) + 30\text{B}_\text{g}(\text{R}) + 29\text{A}_\text{u}(\text{IR}) + 28\text{B}_\text{u}(\text{IR}). \quad (1)$$

Here subscripts g and u denote symmetric and antisymmetric modes with respect to the center of inversion, A and B represent symmetric and antisymmetric C_2 rotation around the $\hat{b}$ axis, and R and IR represent Raman and infrared active modes. Phonon dispersions of LP-En along an itinerary in the first BZ are displayed in Figure 2. The LO-TO splitting in the LP-En is clearly seen in Figure 2 along the C-Γ-Y segment. Two gaps appear in the dispersion curves. The lowest group of modes that range from 0 to ~600 cm^{-1} mainly involves motions corresponding to "wiggling" of the S chain and O chain (resulting from oxygen displacement of the shared corner in the tetrahedral chains), rotation modes around the $\hat{c}$ axis, translation modes along the $\hat{c}$ axis, and translation modes of magnesium atoms. Modes between ~600 and ~800 cm^{-1} comprise O-Si-O bond-bending displacements which result in SiO_4 tetrahedral distortions. The magnesium atoms in these modes are silent. At ~880 cm^{-1} the Si-O bond-stretching modes inside the SiO_4 tetrahedra start to mix into the O-Si-O bond bending modes until above 1000 cm^{-1} stretching modes dominate. We are particularly interested in phonon modes related with the LP-En to HP-En transition. Figures 3a–3c show the lowest two A_g modes (125.8 and 148.8 cm^{-1}) and one A_u mode (126.5 cm^{-1}) at 0 GPa in LP-En. A close inspection of the lowest two A_g modes shows that they both rotate the S chain away from the O chain when viewed along the $\hat{a}$ axis. This can convert the S chain into the O chain (by changing the O_3-O_3-O_3 angle from 205° to 134° in Figure 1). The effect of the lowest A_g mode displacement on enthalpy change in LP-En was analyzed by *Yu and Wentzcovitch* [2009]. The lowest A_u mode (Figure 3c) represents the "gliding" motion of tetrahedral chains along $\hat{b}$, which affects each chain as a whole and does not affect the chain angles.

[9] The primitive cell of HP-En contains 4 formula units (20 atoms). This leads to 60 normal modes in the BZ, among which 3 are acoustic (1 LA and 2 TA) and 57 are optical (19 LO and 38 TO) as shown in Figure 4. The optical modes at the BZ center may be divided by symmetry as

$$\Gamma^{\text{disp}} = 14\text{A}_\text{g}(\text{R}) + 16\text{B}_\text{g}(\text{R}) + 13\text{A}_\text{u}(\text{IR}) + 14\text{B}_\text{u}(\text{IR}). \quad (2)$$

The phonon dispersion of HP-En is shown in Figure 4 in which the LO-TO splitting can be seen along the A-Γ-N segment. In contrast to LP-En, the phonon dispersion of HP-En shows 3 gaps. The lowest 44 bands with frequencies from 0 to ~600 cm^{-1} are dominated by the magnesium translation modes and the translation and rocking modes of silicate chains. The high-frequency modes of HP-En are similar to those of LP-En. The five modes between ~600 and ~800 cm^{-1} result from O-Si-O bond bending modes with magnesium motions significantly reduced. Modes between ~800 and ~1000 cm^{-1} are represented by a mixture of

Table 2. Calculated (LDA) and Experimentally Measured Atomic Coordinates for LP-En (0 GPa) and HP-En (7.9 GPa) in $MgSiO_3$[a]

	x	y	z
		LP-En	
Mg1 (4e)	0.2516 (0.2511)	0.6555 (0.6533)	0.2140 (0.2177)
Mg2 (4e)	0.2571 (0.2558)	0.0154 (0.0131)	0.2112 (0.2146)
SiA (4e)	0.0425 (0.0433)	0.3419 (0.3408)	0.2963 (0.2944)
SiB (4e)	0.5547 (0.5533)	0.8373 (0.8371)	0.2248 (0.2300)
O1A (4e)	0.8649 (0.8667)	0.3397 (0.3396)	0.1885 (0.1851)
O2A (4e)	0.1226 (0.1228)	0.5030 (0.5009)	0.3194 (0.3218)
O3A (4e)	0.1070 (0.1066)	0.2829 (0.2795)	0.6198 (0.6153)
O1B (4e)	0.3764 (0.3762)	0.8384 (0.8399)	0.1204 (0.1247)
O2B (4e)	0.6341 (0.6340)	0.9829 (0.9825)	0.3908 (0.3891)
O3B (4e)	0.6082 (0.6053)	0.6901 (0.6942)	0.4449 (0.4540)
		P-En	
Mg1 (4e)	0 (0)	0.9076 (0.9057)	0.25 (0.25)
Mg2 (4e)	0 (0)	0.2749 (0.2742)	0.25 (0.25)
Si (8f)	0.3001 (0.2988)	0.0920 (0.0915)	0.2088 (0.211)
O1 (8f)	0.1215 (0.1215)	0.0908 (0.0914)	0.1379 (0.139)
O2 (8f)	0.3775 (0.380)	0.2383 (0.2376)	0.3696 (0.367)
O3 (8f)	0.3583 (0.357)	0.0624 (0.0613)	0.9092 (0.915)

[a]Experimentally measured values are in parentheses; 4e and 8f denote atomic Wyckoff positions in a crystal structure.

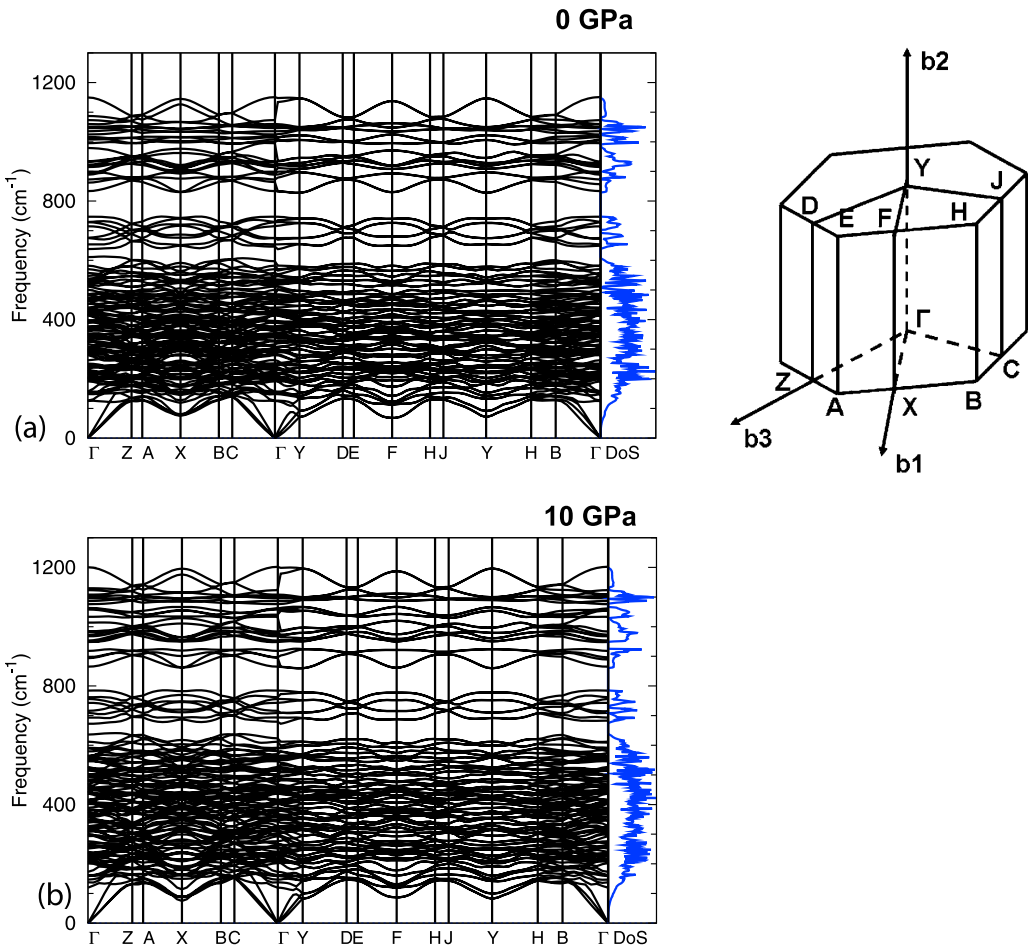

Figure 2. Phonon dispersions and vibrational density of states of LP-En at (a) 0 GPa and (b) 10 GPa in the first Brillouin zone.

O-Si-O bond bending and Si-O bond stretching motion. Those above 1000 cm^{-1} result from pure Si-O bond stretching modes. Figures 3d–3g show four typical low-frequency modes in HP-En at 12.5 GPa. The lowest B_g mode (162.7 cm^{-1} Figure 3d) involves sliding of the silicate chains along the $\hat{b}$ axis and magnesium translations along the $\hat{a}$ axis. The A_g mode (184.3 cm^{-1} Figure 3e) is dominated by chain translation approximately along the $\hat{c}$ axis especially for silicon atoms, and the B_u mode (225.0 cm^{-1} Figure 3f) represents O chain rocking modes around the $\hat{c}$ axis. The A_g mode (245.6 cm^{-1} Figure 3g) mainly consists of magnesium vibrations in the *b*-*c* plane with the silicate chains oscillating out of phase along the $\hat{a}$ axis.

[10] The calculated Raman and IR frequencies of LP-En at ambient pressure and HP-En at 12.5 GPa are in good agreement with the experimental measurements of *Chopelas* [1999] and *Lin* [2004] (Tables 3 and 4), at least in the low- and high-frequency regimes. In the intermediate frequency regime, 660–840 cm^{-1} of LP-En and 450–710 cm^{-1} for HP-En, the agreement is slightly worse but still within 2% of the experimental wave number (e.g., LP-En A_g modes 46, 48, and 49 in Table 3 and HP-En A_g mode 14 and 20 in Table 4). For HP-En note that the calculated Raman frequencies lie between two sets of measurements [*Chopelas*, 1999; *Lin*, 2004]. The calculated IR frequencies can supplement experimental data.

4. Thermodynamic Properties

[11] Within the QHA, the Helmholtz free energy is expressed as

$$F(V,T) = U_0(V) + \frac{1}{2}\sum_{\mathbf{q},j}\hbar\omega_j(\mathbf{q},V) + k_BT\sum_{\mathbf{q},j}\ln\left[1-\exp\left(-\hbar\omega_j(\mathbf{q},V)/k_BT\right)\right], \quad (3)$$

where the first term is the static internal energy, the second is zero point motion, and the third is harmonic vibrational contributions. The summation is taken on a 8 × 8 × 8 q point mesh which contains only 30(24) points in the irreducible wedge of the first BZ of LP-En (HP-En). The parameter $\omega_j(\mathbf{q}, V)$ represents the *j*th branch lattice vibrational frequency with wave vector $\mathbf{q}$ in a periodic crystal with unit cell volume V. These phonon frequencies are calculated following structure relaxations for each volume (or pressure). The QHA is expected to work within its validity limit.

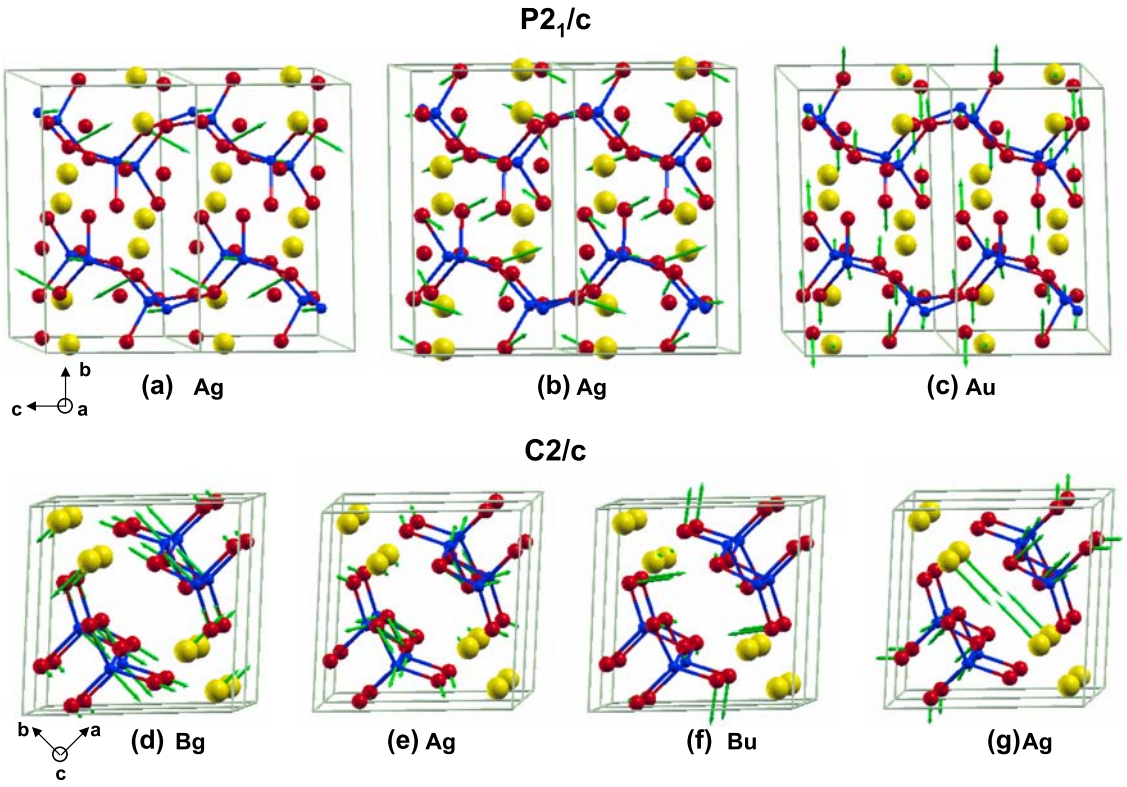

Figure 3. Illustration of some normal modes of LP-En ($P2_1/c$) at 0 GPa for (a) A_g mode with vibrational frequency 125.8 cm^{-1}, (b) A_g 148.8 cm^{-1}, and (c) A_u 126.5 cm^{-1}, and HP-En (C2/c) at 7 GPa for (d) B_g mode with vibrational frequency 162.7 cm^{-1}, (e) A_g 184.3 cm^{-1}, (f) B_u 225.0 cm^{-1}, and (g) A_g 245.6 cm^{-1}.

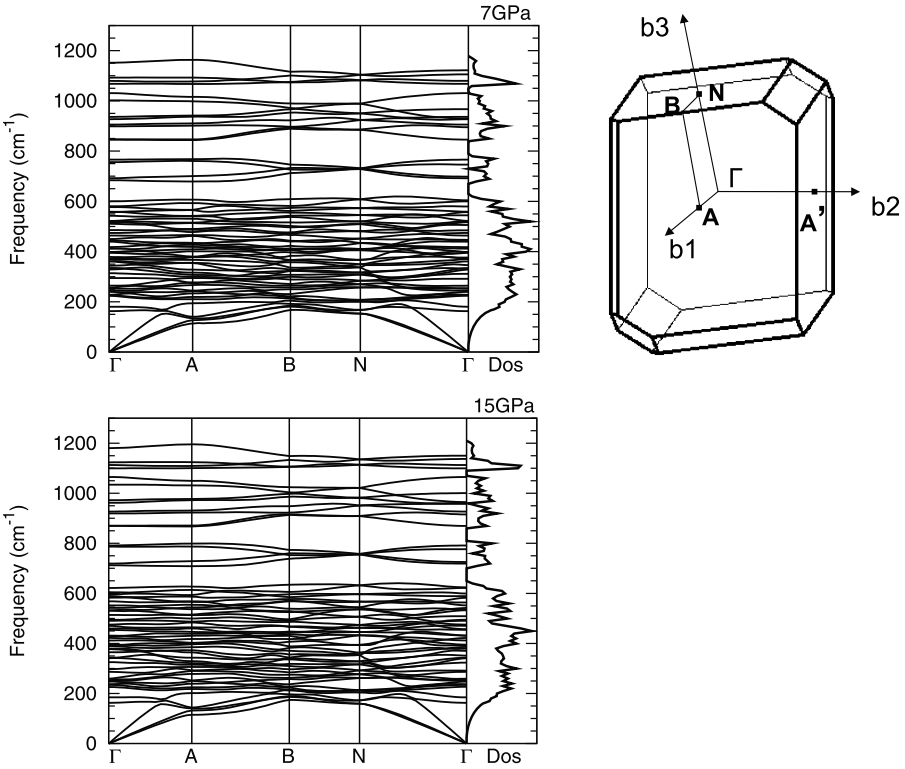

Figure 4. Phonon dispersions and vibrational density of states of HP-En at 7 GPa and 15 GPa in the first Brillouin zone.

Table 3. Calculated Raman and IR Frequencies for LP-En ($P2_1/c$) Compared With Experimental Data at Ambient Pressure[a]

Raman				IR		
Mode	Calc	Exp	Mode	Mode	Calc	Mode
1	125.8	121 m	A_g	1	126.5	A_u
2	148.8	143 m	A_g	2	155.6	B_u
3	153.2		B_g	3	203.0	A_u
4	154.0		A_g	4	204.8	B_u
5	157.8	158 m	B_g	5	216.4	B_u
6	191.1		B_g	6	218.5	A_u
7	197.0	195 m	A_g	7	224.4	A_u
8	202.8	206 m	B_g	8	240.4	B_u
9	202.9		A_g	9	244.4	A_u
10	210.1		A_g	10	262.4	B_u
11	229.9		A_g	11	284.0	B_u
12	234.4	233 w	B_g	12	285.2	A_u
13	246.4	245 ms	B_g	13	292.2	A_u
14	250.8		A_g	14	297.9	B_u
15	279.7	279 w	A_g	15	302.7	B_u
16	292.0		B_g	16	316.7	A_u
17	297.7		B_g	17	323.8	B_u
18	307.6	304 w	A_g	18	337.1	B_u
19	327.0	324 mw	B_g	19	350.6	B_u
20	329.6		A_g	20	351.6	A_u
21	340.5		B_g	21	360.2	A_u
22	342.0	344 s	A_g	22	374.0	B_u
23	349.3		B_g	23	377.3	A_u
24	363.4		A_g	24	390.2	A_u
25	371.3	371 ms	B_g	25	416.5	B_u
26	371.7		A_g	26	418.7	A_u
27	390.2	388 w	B_g	27	419.8	B_u
28	395.3	405 m	B_g	28	425.0	B_u
29	414.7	418 m	B_g	29	429.0	A_u
30	415.2		A_g	30	453.4	A_u
31	422.5		A_g	31	462.8	B_u
32	433.4	432 m	A_g	32	464.8	A_u
33	440.6		B_g	33	471.9	A_u
34	452.9	453 w	A_g	34	476.8	B_u
35	463.7		B_g	35	484.1	A_u
36	485.7	480 w	B_g	36	502.0	B_u
37	500.7		A_g	37	511.4	A_u
38	517.8		A_g	38	528.1	A_u
39	520.6	523 m	B_g	39	529.1	B_u
40	527.5		B_g	40	549.0	B_u
41	535.4		A_g	41	557.6	A_u
42	547.4	557 w	A_g	42	636.7	B_u
43	570.2		B_g	43	669.4	B_u
44	582.1	583 mw	B_g	44	714.6	A_u
45	653.8	666 s	A_g	45	728.7	A_u
46	675.0	689 vs	A_g	46	832.8	B_u
47	729.4		B_g	47	872.7	A_u
48	747.0	755 mw	B_g	48	894.4	A_u
49	833.4	848 mw	A_g	49	914.9	A_u
50	888.7		B_g	50	923.8	B_u
51	899.0		B_g	51	935.1	B_u
52	920.7		A_g	52	995.6	A_u
53	922.8	927 mw	B_g	53	1003.9	B_u
54	932.7		A_g	54	1024.9	A_u
55	1007.6		A_g	55	1054.3	B_u
56	1015.7	1012 vs	B_g	56	1073.2	A_u
57	1035.7	1034 s	A_g	57	1147.8	B_u
58	1046.3		A_g			
59	1050.6		B_g			
60	1060.0		B_g			

[a]Calculated Raman and IR frequencies are in cm^{-1}. Experimental results are from *Lin* [2004], with the abbreviations s, sharp; w, wide; v, very; m, medium.

Superlinear and sublinear deviations from the thermal expansivity at high temperature serve as markers of this limit [*Wentzcovitch et al.*, 2004; *Carrier et al.*, 2007].

[12] The fundamental thermodynamic quantities are derived after fitting a third-order finite strain equation of state to the calculated free energy versus volume at each temperature. Figure 5a shows the calculated isothermal compression curves of LP-En and HP-En compared with experimental data [*Angel and Hugh-Jones*, 1994; *Kung et al.*, 2004]. For both phases, the agreement with experimental measurements at room temperature is excellent. At 7 GPa, which is near the experimental transition pressure, the volume difference ($\Delta V/\overline{V}$) between LP-En and HP-En is about 2.8%. The adiabatic bulk moduli of LP-En and HP-En, derived from a third-order Birch-Murnaghan equation of state, are compared with experimental values in Figure 5b. The calculated K'_T are 5.5 for LP-En and HP-En at ambient conditions, which agree quite well with data obtained by *Kung et al.* [2004]. The absolute values of the bulk moduli from this study are also close to room temperature experimental measurements especially at high pressures (e.g., $\geq$10 GPa, Figure 5b). Given the uncertainties in experimental fitting (due to the small compression range),

Table 4. Calculated Raman and IR Frequencies for HP-En (C2/c) at Compared With Experimental Data at 12.5 GPa[a]

Raman					IR		
Mode Number	Calc	Exp 1	Exp 2	Mode	Mode Number	Calc	Mode
		152.8[b]					
1	162.7	161.1	170.0	B_g	1	225.0	B_u
2	184.3	185.3	185.5	A_g	2	245.6	A_u
3	231.9			B_g	3	255.1	B_u
4	234.6	237.8	238.4	A_g	4	280.7	B_u
5	249.6	248.9	249.4	B_g	5	320.6	A_u
6	257.5	264.2	263.9	A_g	6	344.4	B_u
7	290.5	279.0		B_g	7	378.2	A_u
8	337.7			B_g	8	380.0	B_u
9	341.7	341.2	341.6	A_g	9	384.6	A_u
10	363.2	375.1	368.8	B_g	10	418.2	A_u
11	388.7			A_g	11	425.6	B_u
12	406.6	403.6	407.4	A_g	12	442.7	A_u
13	416.0	410.2		B_g	13	464.8	B_u
14	452.3	433.2	447.6	A_g	14	501.7	A_u
15	462.3	450.3		B_g	15	530.2	B_u
16	481.5			B_g	16	533.5	A_u
17	488.2	490.1	487.5	A_g	17	533.4	B_u
18	504.8			A_g	18	574.3	B_u
19	542.6	542.0	541.5	B_g	19	579.1	A_u
20	575.6	563.2	571.0	B_g	20	698.4	B_u
21	593.2	576.2		A_g	21	767.1	A_u
22	614.7	626.1		B_g	22	862.8	B_u
23	710.7	722.5	720.9	A_g	23	909.2	A_u
24	783.5	786.7	787.4	B_g	24	953.9	A_u
25	862.0	863.3	865.8	A_g	25	987.5	B_u
26	920.5	917.4		B_g	26	1103.0	B_u
27	951.2	944.2	942.4	B_g	27	1127.8	A_u
28	1054.8	1060.1	1062.3	A_g			
29	1090.1	1092.2	1089.0	A_g			
30	1105.9			B_g			

[a]Calculated Raman and IR frequencies are in cm^{-1}. Exp 1 is from *Lin* [2004] and exp 2 is from *Chopelas* [1999].

[b]One experimental Raman frequency that is not observed from calculation but listed for comparison purpose.

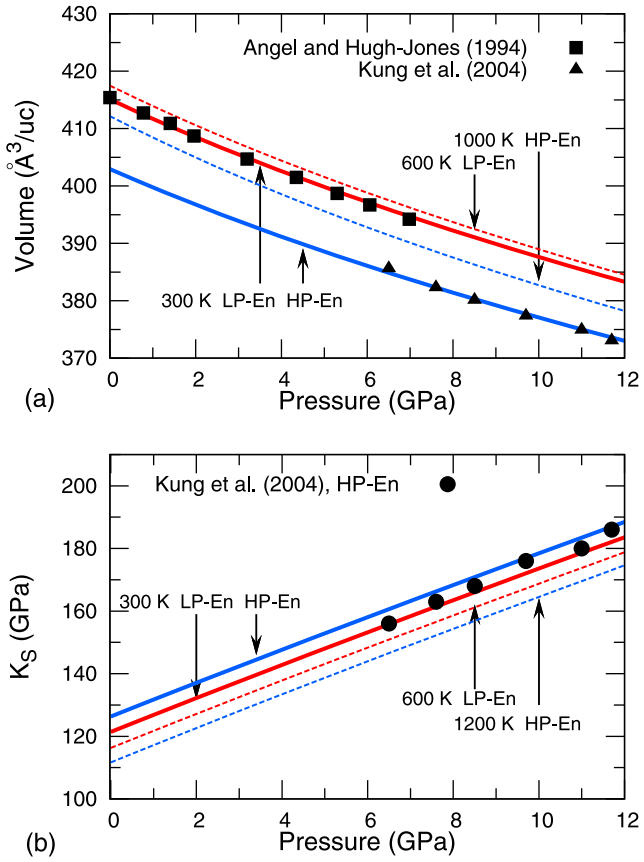

Figure 5. (a) Compression curves of LP-EN (red) along 300 and 600 K isotherms and those of HP-EN (blue) along 300 and 1000 K isotherms (40 atoms per unit cell). Squares represent 300 K experimental data of LP-En by *Angel and Hugh-Jones* [1994], and triangles represent experimental data of HP-En by *Kung et al.* [2004]. (b) Pressure dependence of adiabatic bulk moduli of LP-En (red) along 300 and 600 K isotherms and that of HP-En along 300 and 1200 K isotherms compared with room temperature measurements by *Kung et al.* [2004].

the agreement between calculation and experiments is very good.

[13] Table 5 compares calculated and experimentally determined thermal expansivities and heat capacities for LP-En and HP-En at room condition. The thermal expansion coefficient, $\alpha = 1/V(\partial V/\partial T)_P$, is determined numerically from the equilibrium volume variation with respect to temperature at each pressure (Figure 6). Take HP-En for example, at 0 GPa and 300 K. Calculation shows $\alpha = 2.5 \times 10^{-5}$ K^{-1} which is close to experimentally determined 2.64×10^{-5} K^{-1} by *Shinmei et al.* [1999]. At constant temperature, α decreases substantially with increasing pressure, e.g., at ~800 K, α at 15 GPa is only one half its value at 0 GPa in HP-En (Figure 6). The absence of any strong deviation of the α versus T curve from the linear behavior in either LP-En or HP-En phases indicates that anharmonicity in LP-En and HP-En may be unimportant even at low pressures. The calculated temperature dependence of heat capacity for LP-En at ambient pressure is in good agreement with data measured by *Krupka et al.* [1985]. We also show the temperature dependence of entropy and thermal Grüneisen parameter (defined by $\gamma_{th} \equiv \alpha K_S V/C_P = \alpha K_T V/C_V$) at various pressures. These quantities have not yet been determined experimentally.

5. LP-En to HP-En Phase Transition

[14] In experiments, the $MgSiO_3$ LP-En ($P2_1/c$) to HP-En (C2/c) transition is found to be nonquenchable and reversible. At room temperature, *Angel and Hugh-Jones* [1994] show that the transition from $P2_1/c$ to C2/c happens at ~8.0 GPa and the inversion back to $P2_1/c$ at ~5.3 GPa in single crystals under hydrostatic conditions. In powder samples under potentially nonhydrostatic conditions, the hysteresis can extend from 4.0 to 10.7 GPa even at elevated temperatures [*Shinmei et al.*, 1999]. Therefore direct in situ measurements [*Shinmei et al.*, 1999] have not provided any further experimental constraints on the position of the boundary in $MgSiO_3$ enstatite. While the $P2_1/c$ to C2/c transition has very little hysteresis in the $FeSiO_3$ analog system, ferrosilite [*Hugh-Jones et al.*, 1994; *Ross and Reynard*, 1999], and in the Fe-rich members of the solid solution, extrapolation of the transition pressure from ferrosilite to enstatite is tentative and not necessarily reliable [*Ross and Reynard*, 1999]. However, the position of the invariant point between $P2_1/c$, Pbca, and C2/c phases in $MgSiO_3$ can be constrained experimentally by the intersection of the quenchable transition between the $P2_1/c$ and Pbca phases and the Pbca to C2/c transition. The most recent analysis of all of the available data by *Ulmer and Stalder* [2001] places the triple point at 6.6 GPa and 1093 K with an uncertainty of ±0.3 GPa and ±25 K (see the cross in Figure 8).

[15] The QHA-based phase boundary calculation avoids the problem of kinetics because it simply compares the Gibbs free energy of the two transforming phases. Figure 7

Table 5. LDA Calculated Equation of State Parameters and Some Thermodynamic Properties of LP-En and HP-En Compared With Experimental Determinations

	LP-En (300 K, 0 GPa)		HP-En (300 K, 0 GPa)	
	Calc	Exp	Calc	Exp
V_0 (Å^3/(8 $MgSiO_3$))	415.2	414.6(1)[a], 415.4(5)[b]	403.0	405.1(1.7)[b]
K_T (GPa)	121.4	111.1(3.3)[a], 108.5(6.3)[b]	126.3	122.8(16.5)[a], 106.4(17.4)[b]
K'_T	5.5	6.6(1.1)[a], 4.5(1.3)[b]	5.5	5.6(2.9)[a], 5.4(2.7)[b]
α (10^{-5} K^{-1})	2.5		2.46	2.64[b]
C_P (J mol^{-1} K^{-1})	81.67		81.1	81.95[c]

[a] *Angel and Hugh-Jones* [1994].
[b] *Shinmei et al.* [1999].
[c] *Krupka et al.* [1985].

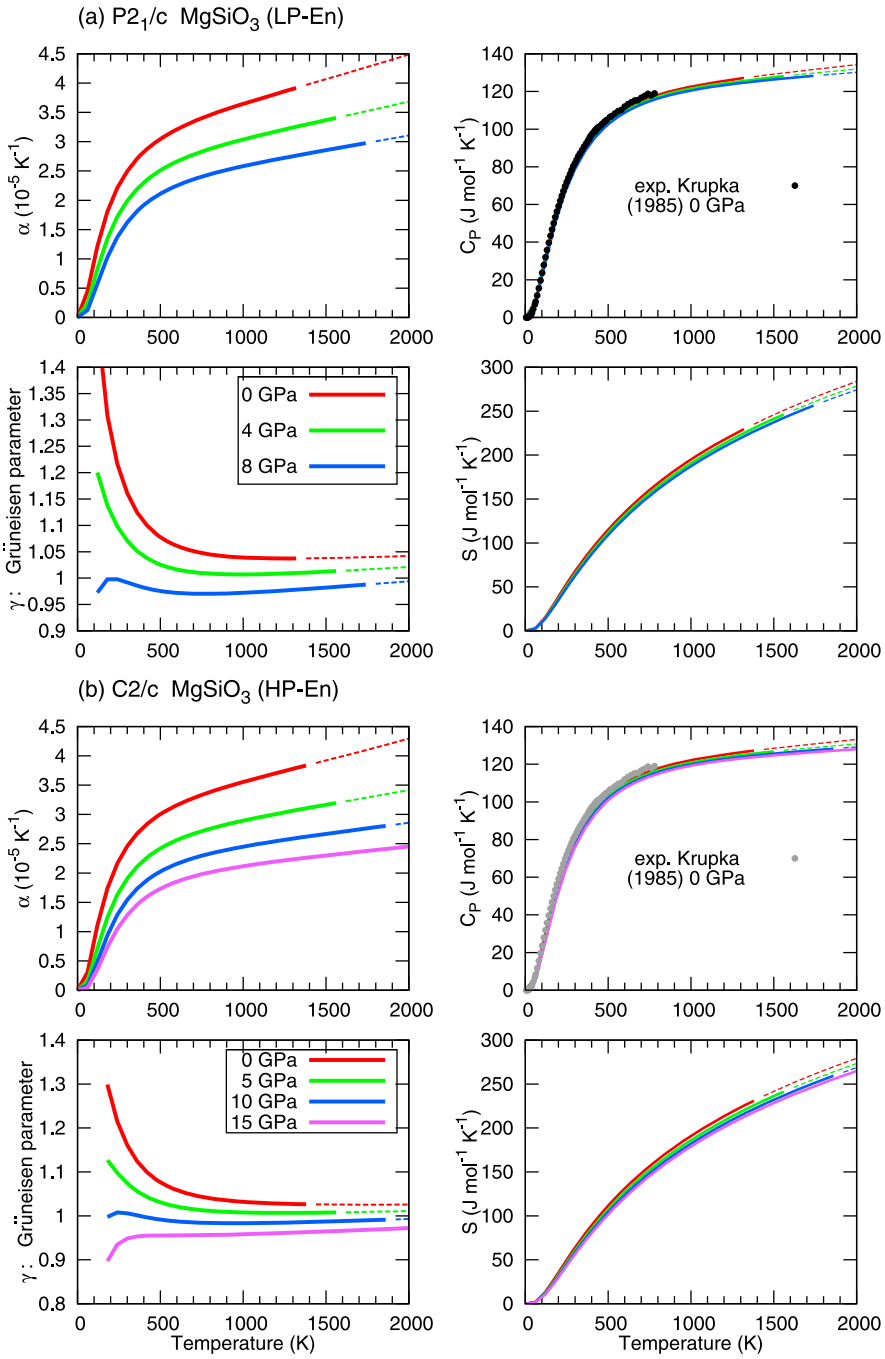

Figure 6. Temperature dependence of thermal expansion coefficient, constant pressure heat capacity, Grüneisen parameter, and entropy of (a) LP-En along 0, 4, and 8 GPa isobars and (b) HP-En along 0, 5, 10, and 15 GPa isobars. Experimental data are from *Krupka et al.* [1985].

shows the variation with pressure of the static enthalpy differences between HP-En and LP-En calculated by the LDA and the GGA functionals. The GGA transition pressure is 7.3 GPa while the LDA yields 1.8 GPa. This is a consequence of differences between the LDA and GGA functional forms [*Lundqvist and March*, 1983]. The calculated transition pressure is sensitive to the total energy convergence. The uncertainty in the phase transition pressure should be within 0.7 GPa (estimated from $\delta P = \delta H/(d\Delta H/dP)$ with $\Delta H \approx \Delta E = 1.5 \times 10^{-4}$ Ry atom^{-1} in section 2 and $dH/dP = 2.4 \times 10^{-4}$ Ry GPa^{-1} atom^{-1} in Figure 7). Including phonon vibrational density of states into the Gibbs free energy yields the phase boundary between LP-En and HP-En (Figure 8). The Clapeyron slopes derived from the LDA and GGA phase boundaries are both 2.9 MPa K^{-1} at 1100 K. Both the experimental triple point and the room temperature hysteresis loop are bracketed by the LDA and GGA phase boundaries, as expected, but neither suffices to constrain the exact position of the boundary.

[16] However, a combination of experimental constraints and the Clapeyron slope obtained from the QHA calculation can provide a much tighter constraint on the position of the boundary. For example, when the room temperature $P2_1/c$ to C2/c transition hysteresis loop [*Angel and Hugh-Jones*, 1994] is used together with the calculated GGA Clapeyron slope, 2.9 MPa K^{-1}, the constrained high-temperature phase boundary between $P2_1/c$ and C2/c should lie in the green shaded parallelogram shown in Figure 8. Thus, if the calculated GGA Clapeyron slope of this transition is correct, then the triple point would be shifted up in pressure by at least 1 GPa relative to current estimate from *Ulmer and Stalder* [2001]. This may have implications for the interpretation of microstructures in pyroxenes exhumed from above subduction zones [*Bozhilov et al.*, 1999].

6. Conclusions

[17] Density functional based pseudopotential calculations have been successfully applied to the phase transition between low-pressure ($P2_1/c$) and high-pressure (C2/c) clinoenstatite in $MgSiO_3$. With an improved magnesium pseudopotential and complete phonon calculations using density functional perturbation theory, this calculation has significantly improved the agreement between calculated and experimentally measured room temperature crystal structure parameters and the thermodynamic equation of state. Good agreement between the calculated Raman and IR frequencies and those from experimental measurements confirm the accuracy of this calculation. Lattice vibrational analysis shows that at least two low frequency A_g modes may be implicated in the LP- to HP-En transition. Finally the phase boundary calculations show the usual trend displayed by the LDA and the GGA functionals, with LDA underestimating the phase transition pressure while GGA overestimating it. They bracket experimentally determined triple point for the LP-En, HP-En, and orthoenstatite. Using the calculated Clapeyron slope and the room temperature hysteresis loop in LP-HP transition from *Angel and Hugh-Jones* [1994], we suggest that the experimentally estimated triple point may be shifted up in pressure by at least 1 GPa.

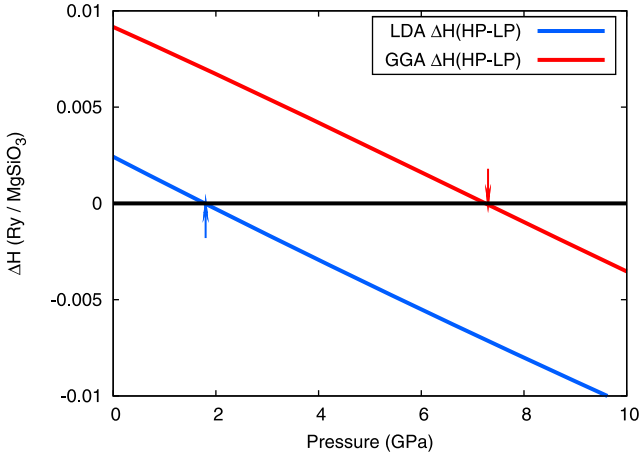

Figure 7. Static enthalpy differences (0 K) between LP-En and HP-En versus pressure calculated by the LDA and GGA. Static transition pressures are indicated by arrows: 1.8 GPa (LDA) and 7.3 GPa (GGA).

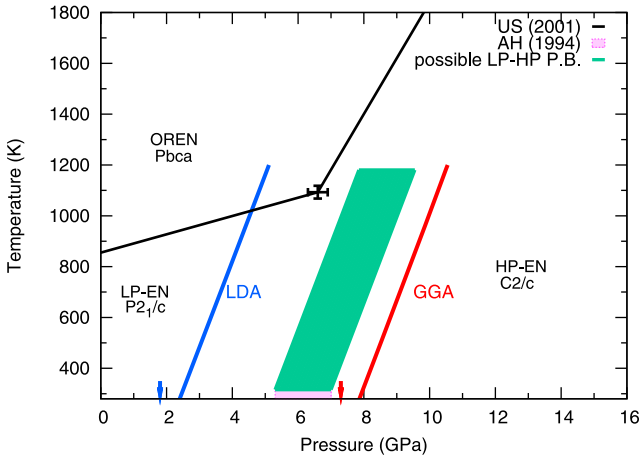

Figure 8. Temperature versus pressure phase diagram of LP-En ($P2_1/c$), HP-En (C2/c), and OREN (Pbca, orthoenstatite) in $MgSiO_3$. The blue and red solid lines represent LDA and GGA phase boundaries for $P2_1/c \rightleftharpoons C2/c$ transition, respectively. The calculated Clapeyron slope at 1100 K is 2.9 MPa K^{-1} (by both LDA and GGA). The static transition pressures are indicated by arrows (from Figure 7). The black lines labeled by US(2001) represent high-temperature experimental phase boundaries between $P2_1/c$ and Pbca, and Pbca $\rightleftharpoons$ C2/c by *Ulmer and Stalder* [2001] with the triple point being at 7.6 GPa, 1093 K. Error bars indicate the experimental uncertainties. The pink shaded bar labeled by AH(1994) represents room temperature $P2_1/c$ to C2/c transition pressure hysteresis loop reported by *Angel and Hugh-Jones* [1994]. The green shaded area represents possible $P2_1/c$ to C2/c phase boundary deduced by a combination of DFT-QHA calculated Clapeyron slope and room temperature hysteresis (in pink shaded bar). Stability field of protoenstatite is ignored.

[18] **Acknowledgments.** This research was supported by NSF grants EAR-0230319, EAR-0635990, and ATM-0428774. Computations were performed at the Minnesota Supercomputing Institute. R.M.W. acknowledges the Humboldt Foundation for support and the hospitality of Björn Winkler at the Institute of Geosciences, Mineralogy, and Crystallography, University of Frankfurt, during the preparation of this manuscript.

References

Akaogi, M., and S. Akimoto (1977), Pyroxene-garnet solid-solution equilibria in the systems $Mg_4Si_4O_{12}$-$Mg_3Al_2Si_3O_{12}$ and $Fe_4Si_4O_{12}$-$Fe_3Al_2Si_3O_{12}$ at high pressures and temperatures, *Phys. Earth Planet. Inter.*, *15*, 90–106, doi:10.1016/0031-9201(77)90013-9.

Angel, R. J., and D. A. Hugh-Jones (1994), Equations of state and thermodynamic properties of enstatite pyroxenes, *J. Geophys. Res.*, *99*, 19,777–19,783, doi:10.1029/94JB01750.

Angel, R. J., A. Chopelas, and N. L. Ross (1992), Stability of high-density clinoenstatite at upper-mantle pressures, *Nature*, *358*, 322–324, doi:10.1038/358322a0.

Baroni, S., S. de Gironcoli, A. D. Corso, and P. Giannozzi (2001), Phonons and related crystal properties from density-functional perturbation theory, *Rev. Mod. Phys.*, *73*, 515–562, doi:10.1103/RevModPhys.73.515.

Bozhilov, K. N., H. W. Green II, and L. Dobrzhinetskaya (1999), Clinoenstatite in Alpe Arami peridotite: Additional evidence of very high pressure, *Science*, *284*, 128–132, doi:10.1126/science.284.5411.128.

Capillas, C., E. Kroumova, M. I. Aroyo, J. M. Perez-Mato, H. T. Stokes, and D. M. Hatch (2003), SYMMODES: A software package for group-theoretical analysis of structural phase transitions, *J. Appl. Cryst.*, *36*(3), 953–954, doi:10.1107/S0021889803003212.

Carrier, P., R. Wentzcovitch, and J. Tsuchiya (2007), First-principles prediction of crystal structures at high temperatures using the quasi-

harmonic approximation, *Phys. Rev. B*, *76*(6), 064116, doi:10.1103/PhysRevB.76.064116.
Ceperley, D. M., and B. J. Alder (1980), Ground state of the electron gas by a stochastic method, *Phys. Rev. Lett.*, *45*, 566–569, doi:10.1103/PhysRevLett.45.566.
Chopelas, A. (1999), Estimates of mantle relevant Clapeyron slopes in the $MgSiO_3$ system from high-pressure spectroscopic data, *Am. Mineral.*, *84*, 233–244.
Chopelas, A., and R. Boehler (1992), Raman spectroscopy of high pressure $MgSiO_3$ phases synthesized in a CO_2 laser heated diamond anvil cell: Perovskite and clinopyroxene, in *High Pressure Research: Application to Earth and Planetary Sciences*, edited by Y. Syono and M. Manghnani, pp. 101–108, Terra Sci., Tokyo.
Choudhury, N., S. Ghose, C. P. Chowdhury, C. K. Loong, and S. L. Chaplot (1998), Lattice dynamics, Raman spectroscopy, and inelastic neutron scattering of orthoenstatite $Mg_2Si_2O_6$, *Phys. Rev. B*, *58*(2), 756–765, doi:10.1103/PhysRevB.58.756.
Dal Corso, A., S. Baroni, R. Resta, and S. de Gironcoli (1993), Ab initio calculation of phonon dispersions in II-VI semiconductors, *Phys. Rev. B*, *47*, 3588–3592, doi:10.1103/PhysRevB.49.5323.
Downs, R. T. (2003), Topology of the pyroxenes as a function of temperature, pressure, and composition as determined from the procrystal electron density, *Am. Mineral.*, *88*(4), 556–566.
Duan, W. H., B. B. Karki, R. M. Wentzcovitch, and B. L. Gu (2001), Ab initio study of $MgSiO_3$ low-clinoenstatite at high pressure, *Am. Mineral.*, *86*, 762–766.
Giannozzi, P., et al. (2009), QUANTUMESPRESSO: A Modular and open-source software project for quantum simulations of materials, *J. Phys. Condens. Matter*, *21*, 5502, doi:10.1088/0953-8984/21/39/395502.
Hugh-Jones, D. A., A. B. Woodland, and R. J. Angel (1994), The structure of high-pressure C2/c ferrosilite and crystal chemistry of high-pressure C2/c pyroxenes, *Am. Mineral.*, *79*, 1032–1041.
Jahn, S. (2008), High-pressure phase transitions in $MgSiO_3$ orthoenstatite studied by atomistic computer simulation, *Am. Mineral.*, *93*(4), 528–532, doi:10.2138/am.2008.2710.
Jahn, S., and R. Martoňák (2008), Plastic deformation of orthoenstatite and the ortho- to high-pressure clinoenstatite transition: A metadynamics simulation study, *Phys. Chem. Miner.*, *35*, 17–23, doi:10.1007/s00269-007-0194-2.
Kanzaki, M. (1991), Ortho/clinoenstatite transition, *Phys. Chem. Miner.*, *17*, 726–730, doi:10.1007/BF00202244.
Karki, B. B., R. M. Wentzcovitch, S. de Gironcoli, and S. Baroni (2000), High-pressure lattice dynamics and thermoelasticity of MgO, *Phys. Rev. B*, *61*, 8793–8800, doi:10.1103/PhysRevB.61.8793.
Kokalj, A. (2003), Computer graphics and graphical user interfaces as tools in simulations of matter at the atomic scale, *Comput. Mater. Sci.*, *28*(2), 155–168, doi:10.1016/S0927-0256(03)00104-6.
Krupka, K. M., B. S. Hemingway, R. A. Robie, and D. M. Kerrick (1985), High-temperature heat capacities and derived thermodynamic properties of anthophyllite, diopside, enstatite, dolomite, bronzite, talc, tremolite, and wollastonite, *Am. Mineral.*, *70*, 261–271.
Kung, J., B. Li, T. Uchida, Y. Wang, D. Neuville, and R. C. Liebermann (2004), In situ measurements of sound velocities and densities across the orthopyroxene–high-pressure clinopyroxene transition in $MgSiO_3$ at high pressure, *Phys. Earth Planet. Inter.*, *147*, 27–44, doi:10.1016/j.pepi.2004.05.008.
Li, L., R. M. Wentzcovitch, D. J. Weidner, and C. R. S. Da Silva (2007), Vibrational and thermodynamic properties of forsterite at mantle conditions, *J. Geophys. Res.*, *112*, B05206, doi:10.1029/2006JB004546.
Lin, C.-C. (2004), Pressure-induced polymorphism in enstatite ($MgSiO_3$) at room temperature: Clinoenstatite and orthoenstatite, *J. Phys. Chem. Solids*, *65*, 913–921, doi:10.1016/j.jpcs.2003.09.028.
Lundqvist, S., and N. M. March (Eds.) (1983), *Theory of the Inhomogeneous Electron Gas*, Plenum Press, New York.
Martoňák, R., D. Donadio, A. R. Oganov, and M. Parrinello (2006), Crystal structure transformations in SiO_2 from classical and ab initio metadynamics, *Nature*, *5*, 623–626, doi:10.1038/nmat1696.
Matsui, M., and G. D. Price (1992), Computer Simulation of the $MgSiO_3$ Polymorphs, *Phys. Chem. Miner.*, *18*, 365–372, doi:10.1007/BF00199417.
Mendelssohn, M. J., and G. D. Price (1997), Computer modelling of a pressure induced phase change in clinoenstatite pyroxenes, *Phys. Chem. Miner.*, *25*, 55–62, doi:10.1007/s002690050086.
Monkhorst, H. J., and J. D. Pack (1976), Special points for Brillouin-zone integrations, *Phys. Rev. B*, *13*, 5188–5192, doi:10.1103/PhysRevB.13.5188.
Ohashi, Y. (1984), Polysynthetically-twinned structures of enstatite and wollastonite, *Phys. Chem. Miner.*, *10*, 217–229, doi:10.1007/BF00309314.
Pacalo, R. E. G., and T. Gasparik (1990), Reversals of the orthoenstatite-clinoenstatite transition at high pressures and high temperatures, *J. Geophys. Res.*, *95*, 15,853–15,858, doi:10.1029/JB095iB10p15853.
Parrinello, M., and A. Rahman (1980), Crystal structure and pair potentials: A molecular-dynamics study, *Phys. Rev. Lett.*, *45*, 1196–1199, doi:10.1103/PhysRevLett.45.1196.
Perdew, J., and A. Zunger (1981), Self-interaction correction to density-functional approximations for many-electron systems, *Phys. Rev. B*, *23*(10), 5048–5079, doi:10.1103/PhysRevB.23.5048.
Perdew, J. P., K. Burke, and M. Ernzerhof (1996), Generalized gradient approximation made simple, *Phys. Rev. Lett.*, *77*, 3865–3868, doi:10.1103/PhysRevLett.77.3865.
Revenaugh, J., and T. H. Jordan (1991), Mantle layering from ScS reverberations. 2. The transition zone, *J. Geophys. Res.*, *96*(B12), 19,763–19,780, doi:10.1029/91JB01486.
Ringwood, A. E. (1967), The pyroxene-garnet transformation in the Earth's mantle, *Earth Planet. Sci. Lett.*, *2*, 255–263, doi:10.1016/0012-821X(67)90138-0.
Ringwood, A. E. (1975), *Composition and Petrology of the Earth's Mantle*, Chap. 14-3, McGraw-Hill, New York.
Ross, N. L., and B. Reynard (1999), The effect of iron on the $P2_1/c$ to C2/c transition in the (Mg, Fe)SiO_3 clinopyroxene, *Eur. J. Mineral.*, *11*, 585–589.
Shimobayashi, N., A. Miyake, M. Kitamura, and E. Miura (2001), Molecular dynamics simulations of the phase transition between low-temperature and high-temperature clinoenstatites, *Phys. Chem. Miner.*, *28*(9), 591–599, doi:10.1007/s002690100192.
Shinmei, T., N. Tomioka, K. Fujino, K. Kuroda, and T. Irifune (1999), In situ X-ray diffraction study of enstatite up to 12 GPa and 1473 K and equations of state, *Am. Mineral.*, *84*(10), 1588–1594.
Troullier, N., and J. L. Martins (1991), Efficient pseudopotentials for plane-wave calculations, *Phys. Rev. B*, *43*, 1993–2006, doi:10.1103/PhysRevB.43.1993.
Tsuchiya, T., J. Tsuchiya, K. Umemoto, and R. M. Wentzcovitch (2004), Phase transition in $MgSiO_3$ perovskite in the Earth's lower mantle, *Earth Planet. Sci. Lett.*, *224*, 241–248, doi:10.1016/j.epsl.2004.05.017.
Ulmer, P., and R. Stalder (2001), The Mg (Fe)SiO_3 orthoenstatite-clinoenstatite transitions at high pressures and temperatures determined by Raman-spectroscopy on quenched samples, *Am. Mineral.*, *86*(10), 1267–1274.
Wentzcovitch, R. M. (1991), Invariant molecular-dynamics approach to structural phase transitions, *Phys. Rev. B*, *44*, 2358–2361, doi:10.1103/PhysRevB.44.2358.
Wentzcovitch, R. M., D. A. Hugh-Jones, R. J. Angel, and G. D. Price (1995), Ab-initio study of $MgSiO_3$ C2/c enstatite, *Phys. Chem. Miner.*, *22*, 453–460, doi:10.1007/BF00200323.
Wentzcovitch, R. M., B. B. Karki, M. Cococcioni, and S. de Gironcoli (2004), Thermoelastic properties of $MgSiO_3$-Perovskite: Insights on the nature of the Earth's lower mantle, *Phys. Rev. Lett.*, *92*(1), 018501, doi:10.1103/PhysRevLett.92.018501.
Woodland, A. B. (1998), The orthorhombic to high-P monoclinic phase transition in Mg-Fe pyroxenes: Can it produce a seismic discontinuity?, *Geophys. Res. Lett.*, *25*(8), 1241–1244, doi:10.1029/98GL00857.
Woodland, A. B., and R. J. Angel (1997), Reversal of the orthoferrosilite-high-P clinoferrosilite transition; a phase diagram for $FeSiO_3$ and implications for the mineralogy of the Earth's upper mantle, *Eur. J. Mineral.*, *9*(2), 245–254.
Wu, Z., and R. M. Wentzcovitch (2007), Vibrational and thermodynamic properties of wadsleyite: A density functional study, *J. Geophys. Res.*, *112*, B12202, doi:10.1029/2007JB005036.
Yu, Y. G., and R. M. Wentzcovitch (2006), Density functional study of vibrational and thermodynamic properties of ringwoodite, *J. Geophys. Res.*, *111*, B12202, doi:10.1029/2006JB004282.
Yu, Y. G., and R. M. Wentzcovitch (2009), Low-pressure clino- to high-pressure clino-enstatite phase transition: A phonon related mechanism, *Am. Mineral.*, *94*(4), 461–466, doi:10.2138/am.2009.3071.
Yu, Y. G., R. M. Wentzcovitch, T. Tsuchiya, K. Umemoto, and D. J. Weidner (2007), First principles investigation of the postspinel transition in Mg_2SiO_4, *Geophys. Res. Lett.*, *34*, L10306, doi:10.1029/2007GL029462.
Yu, Y. G., Z. Wu, and R. M. Wentzcovitch (2008), α-β-γ transformations in Mg_2SiO_4 in Earth's transition zone, *Earth Planet. Sci. Lett.*, *273*, 115–122, doi:10.1016/j.epsl.2008.06.023.

R. J. Angel and Y. G. Yu, Department of Geosciences, Virginia Polytechnic Institute and State University, Derring Hall, Blacksburg, VA 24061-0000, USA. (yonggang@vt.edu)

R. M. Wentzcovitch, Department of Chemical Engineering and Materials Science, Minnesota Supercomputing Institute, University of Minnesota, 421 Washington Ave., SE, Minneapolis, MN 55455, USA.